Journal of Magnetic Resonance 316 (2020) 106770

Contents lists available at ScienceDirect

Journal of Magnetic Resonance

journal homepage: www.elsevier.com/locate/jmr

Assessing spatial resolution, acquisition time and signal-to-noise ratio for commercial microimaging systems at 14.1, 17.6 and 22.3 T

Julia R. Krug [a,b,c,*], Remco van Schadewijk [d], Frank J. Vergeldt [b,c], Andrew G. Webb [e], Huub J.M. de Groot [d], A. Alia [d,f], Henk Van As [b,c], Aldrik H. Velders [a,c,*]

[a] Laboratory of BioNanoTechnology, Wageningen University and Research, Wageningen, the Netherlands
[b] Laboratory of Biophysics, Wageningen University and Research, Wageningen, the Netherlands
[c] MAGNEFY, Wageningen University and Research, Wageningen, the Netherlands
[d] Solid-state NMR, Leiden Institute of Chemistry, Faculty of Science, Leiden University, Leiden, the Netherlands
[e] C.J. Gorter Center for High Field MRI, Department of Radiology, Leiden University Medical Center, Leiden University, Leiden, the Netherlands
[f] Institute for Medical Physics and Biophysics, Leipzig University, Leipzig, Germany

ARTICLE INFO

Article history:
Received 22 April 2020
Revised 27 May 2020
Accepted 4 June 2020
Available online 10 June 2020

Keywords:
Magnetic resonance microscopy
Ultra-high field strength
Signal-to-noise ratio
Limit of detection

ABSTRACT

This work provides a systematic comparison of the signal-to-noise ratio (SNR), spatial resolution, acquisition time and metabolite limits-of-detection for magnetic resonance microscopy and spectroscopy at three different magnetic field strengths of 14.1 T, 17.6 T and 22.3 T (the highest currently available for imaging), utilizing commercially available hardware. We find an SNR increase of a factor 5.9 going from 14.1 T to 22.3 T using 5 mm radiofrequency (saddle and birdcage) coils, which results in a 24-fold acceleration in acquisition time and deviates from the theoretically expected increase of factor 2.2 due to differences in hardware. This underlines the importance of not only the magnetic field strengths but also hardware optimization. In addition, using a home-built 1.5 mm solenoid coil, we can achieve an isotropic resolution of $(5.5\ \mu m)^3$ over a field-of-view of 1.58 mm × 1.05 mm × 1.05 mm with an SNR of 12:1 using 44 signal averages in 58 h 34 min acquisition time at 22.3 T. In light of these results, we discuss future perspectives for ultra-high field Magnetic Resonance Microscopy and Spectroscopy.

1. Introduction

Magnetic Resonance Microscopy (MRM) is typically defined as acquiring images with at least one of the dimensions with sub-100 μm spatial resolution [1–3]. Many MRM applications use high field vertical bore NMR spectrometers with strong gradients to achieve these high resolutions. In addition to providing highly resolved structural information based on the water signal in biological specimens, the spatial distribution of chemical compounds can be obtained using spatially resolved Magnetic Resonance Spectroscopy (MRS). Due to the inherently low spin polarization, MRM and very high resolution MRS suffer from a low signal-to-noise ratio (SNR) compared to other techniques [4] such as microCT [5], fluorescence microscopy and polarized light microscopy [6], and this limits the maximum attainable spatial resolutions. Improvements in spatial resolution are possible by signal averaging at the expense of long experiment times. For MRS, high concentrations (typically in the mM range) of the compound of interest are required due to the low sensitivity.

The SNR can be expressed in terms of B_0, the detector sensitivity given by the B_1 field per unit current I, the number of spins N_s, T the sample temperature, and V_{noise} the noise from coil and sample (Eq. 1) [7].

$$SNR \propto \underset{\mathrm{I}}{[\gamma B_0]} \underset{\mathrm{II}}{\left[\frac{\gamma^2 h^2 B_0 N_S}{16\pi^2 kT}\right]} \underset{\mathrm{III}}{\left[\frac{B_1}{I}\right]} \underset{\mathrm{IV}}{\left[\frac{1}{V_{noise}}\right]} \tag{1}$$

For MRM, cryoprobe technology which reduces the contribution of V_{noise} (IV) is not widely available and unavailable above 500 MHz (11.7 T). The most common way to improve the SNR is simply to move to higher magnetic fields. For example, by going from 14.1 T to 22.3 T, the SNR theoretically increases by a factor of 2.2 due to the relation SNR ~ $B_0^{7/4}$, taking into account the B_0-dependence of the detector sensitivity (III) [8]. However, theoretical improvements of the SNR caused solely by the B_0-increase

* Corresponding authors at: Wageningen University & Research, Laboratory of BioNanoTechnology and Laboratory of Biophysics, Bornse Weilanden 9, 6708WG Wageningen, the Netherlands (J.R. Krug). Wageningen University & Research, Laboratory of BioNanoTechnology, Bornse Weilanden 9, 6708WG Wageningen, the Netherlands (A.H. Velders).

E-mail addresses: julia.krug@wur.nl (J.R. Krug), aldrik.velders@wur.nl (A.H. Velders).

https://doi.org/10.1016/j.jmr.2020.106770
1090-7807/

are challenging to measure experimentally as the hardware, RF-coil quality and technical capabilities of the used NMR systems differ (*cf* Table 1). Several SNR-formulations for comparing coil performances are readily available in the field of Magnetic Resonance. These include localized time-domain SNR (SNR_t) [9], spectral SNR (SNR_f) [9], and image SNR (SNR_i) [10]. For MRI applications, spin sensitivity per unit volume is the most relevant measure [11], and thus image SNR normalized to unit volume ($SNR_{i,v}$) is a useful measure when comparing different MR images. Other MRI parameters such as bandwidth, matrix size, number of signal averages, acquisition time, repetition time and echo time (notably in their respective ratios to the T_1- and T_2- relaxation time) should either be kept constant or taken into account when comparing different experiments [10,12]. In this paper, we took a practical approach of comparing SNR using the same MRI parameters on the same samples and using similar coils (d = 5 mm) at three different magnetic field strengths.

Besides using the increase in sensitivity at the higher magnetic field strength of 22.3 T for higher spatial resolutions, it is well-known that one can also use the increased sensitivity for faster image acquisition, and therefore potentially to image dynamic systems. The acquisition time (t_{acq}) depends on the desired signal-to-noise ratio SNR, coil diameter d, spin-lattice (T_1), spin-spin relaxation times (T_2 or T_2*), and the voxel volume $(\Delta x)^3$ [3,13] (Eq. (2)).

$$t_{acq} \propto (SNR)^2 d^2 \left(\frac{T_1}{T_2}\right) \frac{1.418 \times 10^{-15}}{(\gamma B_0)^{\frac{7}{2}} C} \left(\frac{1}{\Delta x}\right)^6 \quad (2)$$

In this research, we investigate the effect of high to ultra-high magnetic field strengths B_0 on SNR, by comparing volume coils at different field strengths (14.1 T, 17.6 T and 22.3 T) using standard gradient sets of 2–3 T/m and room temperature conditions for RF coils and sample. At the highest field strength of 22.3 T (^{1}H Larmor frequency = 950 MHz), we additionally studied detector sensitivity by comparing a home-built 1.5 mm solenoid coil with a commercial 5 mm birdcage coil. The improved SNR is quantified for all coils and systems and can be used for optimizing acquisition time, spatial resolution and pushing limits for target sample concentrations. In addition, we determine the detection limits of a metabolite at 22.3 T using the 5 mm birdcage coil. We show that the higher SNR obtained at a B_0-field of 22.3 T, combined with an increase in detector sensitivity using our home-built solenoid coil, allows a measurement with a voxel size of $(5.5\ \mu m)^3$. We place our results which are obtained on the highest field strength currently available for MRI including a commercial gradient system of 3 T/m and room temperature coil and sample temperature in perspective with respect to the values achieved by other research groups with highly optimized components such as gradient fields up to 65 T/m [23] and coil temperatures (T_{eff}) down to 28 K [24]. Finally, we discuss possibilities and challenges for ultra-high field MRM and provide an outlook for the next milestone in future magnetic field strengths for MRI.

2. Experimental

2.1. Spectrometer specifications and hardware

The NMR spectrometers used were a 14.1 T system at Wageningen University & Research, a 17.6 T system at Leiden University and the 22.3 T system of the national Dutch NMR facility (uNMR-nl) located at Utrecht University. All systems are equipped with a Micro5 probe and ParaVision 5 (17.6 T) or ParaVision 6.0.1 (14.1 T and 22.3 T) (Bruker, Ettlingen, Germany). Other relevant specifications can be found in Table 1.

On the 17.6 T and 22.3 T systems commercial 5 mm ^{1}H birdcage coils were used, while on the 14.1 T system we used a dual coil (^{1}H/^{2}H) saddle coil, where the ^{1}H is the 5 mm inner saddle coil (all Bruker, Ettlingen, Germany). For the 5 mm birdcage coils, the linear mode is forced by the absence of two rungs at opposite sides of the coil element and thus only linear operation is enabled.

Additionally, we built a customized solenoid coil for the 22.3 T spectrometer for ^{1}H-imaging by hand-winding enamelled copper wire of 0.4 mm diameter around a 1.5 mm capillary with 6 turns, adding to a solenoid length of 2.2 mm. A fixed tuning capacitor (2.5 pF) and a variable matching capacitor (1.5–6 pF) were added to the resonance circuit mounted on a PCB-board and attached to a support, compatible with the Micro5 probe socket, which utilizes its own in-built RF circuitry.

2.2. SNR tests, calculations and Q-factor measurements

To compare the radiofrequency-coils of different systems, a solution of 20% (v/v) H_2O, 80% (v/v) D_2O and 6.3 mM $CuSO_4$ was used (T_1 = 265 ms; $T_{2,apparent}$ = 75 ms @ 22.3 T (Figure S1)). $T_{2,apparent}$ is reported as the T_2 values were determined based on a T_2-map in imaging mode. The T_2 value at the chosen image resolutions is resolution dependent and lower than the intrinsic T_2 value [14]. For the commercial 5 mm coils (saddle and solenoid), the solution was inserted in a 5.0 mm NMR tube (inner diameter (ID) 4.0 mm), while for the 1.5 mm solenoid coil, we used a 1.5 mm capillary (ID 1.0 mm) (Hilgenberg, Germany) sealed with capillary wax (Hampton Research, USA). A Micro5 gradient coil system was used for all experiments (Table 1).

For SNR-tests, a multi-slice spin-echo sequence (MSME) was used with a repetition time (TR) of 1 s, an echo time (TE) of 7 ms and 1 average (NA). The matrix size was set to 256 × 256 with a field-of-view (FOV) of 6 mm × 6 mm, resulting in an in-plane resolution of 23.4 μm × 23.4 μm. The receiver bandwidth was set to 100 kHz (101 kHz @ 17.6 T due to hardware constraints). The slice

Table 1
Hardware overview the 14.1 T, 17.6 T and 22.3 T spectrometers and imaging equipment.

	14.1 T	17.6 T	22.3 T
Magnet bore size	Standard bore (52 mm)	Wide bore (89 mm)	Standard bore (52 mm)
Manufacturer	Bruker		
Instrument type	Avance III	Avance I	Avance III HD
Commercial RF coil	5 mm dual saddle ^{1}H inside ^{2}H outside	5 mm birdcage	5 mm birdcage
Home-built RF coil	–	–	1.5 mm solenoid
Gradient system	Micro5	Micro5	Micro5
Gradient power supply	GREAT 60	BAFPA 40	GREAT 60
$G_{max,\ achievable}$	3 T/m	2 T/m*	3 T/m

* Due to the gradient amplifiers, this gradient set is limited to 2 T/m.

thickness was adjusted to 0.5 mm to achieve an identical receiver gain of 101 to avoid signal clipping on all three spectrometers and thus allow for comparison while maintaining sufficient SNR for quantification at the lowest field strength (see Bruker manual "Microimaging for Avance III systems" [15]).

To calculate the $SNR_{i,v,}$ regions of interest were chosen in the signal area of the image and the noise area of the image and the mean and standard deviations were determined in FIJI/ImageJ [16]. For the region of interest in the noise area, four regions of interest in the corners of the image were selected and the mean and standard deviations were averaged. We calculated the SNR ratios by determining the SNR of the (magnitude data) image and normalising by the volume of a voxel (Eq. (3)) with mean of the signal (μ_S), mean of the noise (μ_N), the standard deviation of the noise (σ_N) and the voxel dimensions in read (d_r), phase (d_p) and slice directions (d_s).

$$SNR_{i,v} = \frac{\mu_S - \mu_N}{\sigma_N} \times \frac{1}{d_r \times d_p \times d_s} \tag{3}$$

The average $SNR_{i,v}$ of three slices is reported for each 5 mm RF coils. For the value of $SNR_{i,v}$ of the 1.5 mm solenoid coil only two slices are used due to the small homogenous B_1 region of the coil. A DC-offset artefact was visible in the image of the 17.6 T. This did not impair the SNR-quantification as the ROI's were chosen outside of the DC offset (line) artefact.

Q-factor measurement on all coils on their respective probe base were performed using the S_{11}-measurement on a network analyser (Agilent Technologies). Each coil and probe combination was tuned and matched prior to each Q-factor measurement. The resulting Q-factor was calculated by:

$$Q = \frac{\omega_0}{\Delta\omega_{0(@-7dB)}} \tag{4}$$

where the bandwidth $\Delta\omega_0$ is measured at the −7 dB level. The Q-factor values of the RF-coil loaded with the reference sample Q_{loaded} deviate by 7% from $Q_{unloaded}$, showing that for the relatively low-conductivity samples used in this study the loss is coil-dominated.

2.3. Metabolite detection limit using localized spectroscopy

As a reference solution for the detection limit measurements, we used 5 mm tubes filled with 100 mM and 10 mM sodium acetate in de-ionized water. The temperature during the measurements was kept at 298 K. The 5 mm birdcage (@ 22.3 T) coil was used.

A localized spectroscopy sequence (PRESS) was used to record a spectrum on a voxel of 125 nL (500 × 500 × 500) μm^3 volume, with TR 1 s, TE 7.2 ms, spectral bandwidth 9.5 kHz and (1) NA 16, t_{acq} 16 s for 100 mM and 10 mM of acetate or (2) NA 512 and t_{acq} 8 min 32 s for 10 mM of acetate. The VAPOR-scheme was used for water suppression, and VAPOR pulse powers were calibrated prior to the PRESS-measurements. The voxel of interest was centred on the acetate concentration by correcting fo the chemical shift. For shim adjustments, the MAPSHIM shim calculation based on a B_0 map was used, followed by (automatic) iterative shimming. A line-broadening of 5 Hz was applied during processing.

2.4. Effect on acquisition time

A piece of Lily root (*Nymphaea odorata*) was fixed in 4% (v/v) formaldehyde. It was then transferred to fomblin, which does not give ^{1}H-MR signal and to avoid susceptibility artefacts at the air-tissue interface [17,18].

A FLASH-2D experiment was recorded at the three spectrometers (14.1 T, 17.6 T and 22.3 T) with a matrix size of 256 × 256 and a field-of-view of 4 mm × 4 mm, resulting in an isotropic spatial resolution of (15.6 μm)^2 with a slice thickness of 100 μm. Other imaging parameters were repetition time (TR) 60 ms, echo time (TE) 4.0 ms (4.4 ms @ 17.6 T due to hardware constraints), flip angle 30° and a receiver bandwidth of 50 kHz. The number of averages was 768, 128, 32, and t_{acq} was 3 h 17 min, 32 min 46 s, 8 min 11 s for 14.1 T, 17.6 T and 22.3 T, respectively. Furthermore, the 5 mm volume RF coils, namely a saddle on the 14.1 T and birdcage coils on the 17.6 T and 22.3 T were used for these experiments. The SNR_i from the magnitude images was determined with

$$SNR_i = \frac{\mu_S - \mu_N}{\sigma_N} \tag{5}$$

with mean of the signal (μ_S), mean of the noise (μ_N), and the standard deviation of the noise (σ_N).

2.5. Spatial resolution

The spatial resolution phantom was prepared using spherical polymer (PMMA) beads called Spheromers® CA40 (Microbeads, Skedsmokorset, Norway) and doped water (6.3 mM $CuSO_4$). The capillary was approximately half-filled with beads, as trapped air bubbles could still be removed during sample preparation when the capillary was not completely filled with beads.

To test a very high spatial resolution, the 1.5 mm solenoid coil was used on the 22.3 T system. A 3D-FLASH sequence was used to obtain a spatial resolution of 5.5 μm × 5.5 μm × 5.5 μm with t_{acq} of 58 h 34 min. Other imaging parameters were TE 5.5 ms, TR 130 ms, NA 44, matrix size 288 × 192 × 192, field-of-view 1.575 mm × 1.050 mm × 1.050 mm and receiver bandwidth 40.761 kHz. The intensity of the (magnitude) image data was plotted using ImageJ [16].

3. Results

3.1. Hardware

Since the available hardware, such as the consoles, available coils and maximum gradient strengths differ between the systems (Table 1) we kept the experimental parameters constant, wherever feasible.

As mentioned earlier, a commercial saddle coil was used on the 14.1 T (Fig. 1A) and a commercial birdcage coil at the 17.6 T (Fig. 1B) and the 22.3 T (Fig. 1C- left). Additionally, we built a solenoid coil with a coil diameter of 1.5 mm to accommodate smaller samples (Fig. 1C – right).

3.2. SNR and Q-factor measurements

The experimental $SNR_{i,v}$ increased with increasing field strengths from 2.2 × 10^4 mm^{-3} at 14.1 T, to 5.9 × 10^4 mm^{-3} at 17.6 T and 1.3 × 10^5 mm^{-3} at 22.3 T using the 5 mm RF volume coils on all three spectrometers (Fig. 2A). This corresponds to a factor of 5.9 from 14.1 T to 22.3 T using 5 mm RF volume coils.

When increasing the detector sensitivity by using a home-built solenoid coil (d = 1.5 mm), the $SNR_{i,v}$ increased further by a factor of 3.5 with respect to the 5 mm birdcage coil at 22.3 T (Fig. 2A). The same image could thus be recorded 12 times faster if the sample geometry allows the same FOV [13]. According to Hoult and Richards [8], experimental comparison of different coils can be achieved by comparing the 90°-pulse lengths at a given power. Comparing the SNR based on the 90°- pulse of the solenoid and the birdcage at 22.3 T, i.e. the ratios $\frac{B_1}{\sqrt{P}}$ [19], an increase of a factor 4 is found.

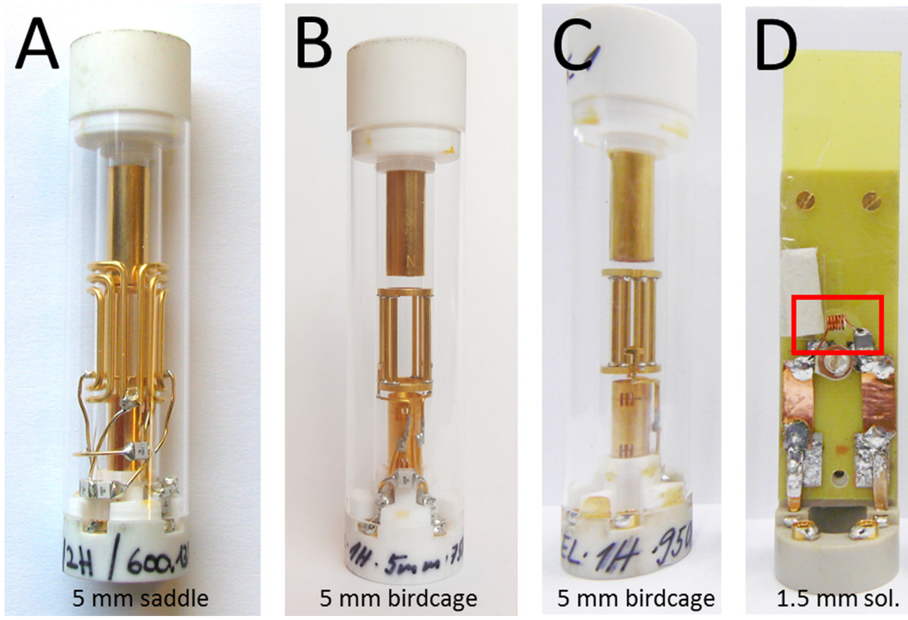

Fig. 1. The exchangeable coil inserts of the different spectrometers are shown. A.) On the 14.1 T spectrometer, a 5 mm 1H/^{2}H dual insert was used with the inner coil being the ^{1}H- saddle coil. B.) The 17.6 T spectrometer was equipped with a 5 mm birdcage coil and C.) for the 22.3 T spectrometer a 5 mm birdcage and D.) a home-built 1.5 mm solenoid coil (red highlight) was used.

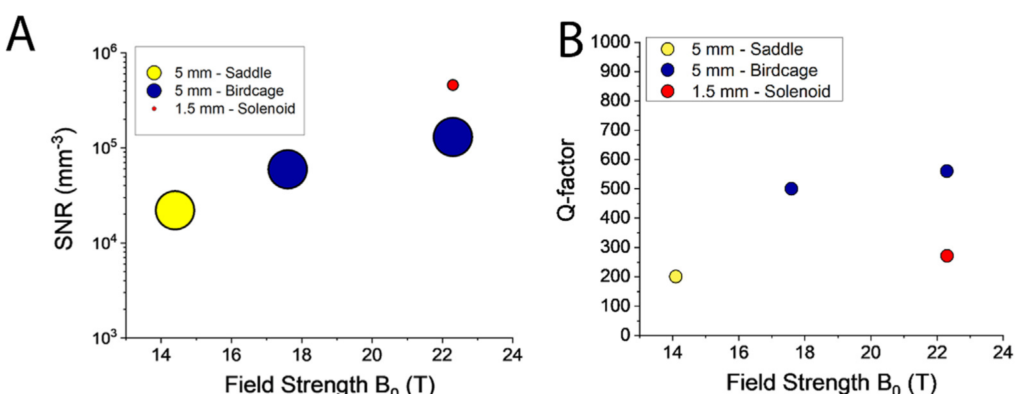

C

B_0	14.1 T	17.6 T	22.3 T	
Coil type	5 mm saddle	5 mm birdcage	5 mm birdcage	1.5 mm solenoid
$SNR_{i,v}$ [mm^{-3}]	2.2 x 10^4	5.9 x 10^4	1.3 x 10^5	4.6 x 10^5
$Q_{unloaded}$ [a.u.]	200	500	561	271

Fig. 2. A) Signal-to-Noise Ratio for different coils at 14.1 T, 17.6 T and 22.3 T shows an $SNR_{i,v}$ increase for the 5 mm volume coils with an increase of B_0 field and an $SNR_{i,v}$ increase for the 1.5 mm solenoid compared to the 5 mm birdcage(@ 22.3 T). B) The Q-factor of all available coils of the different spectrometers were determined. C) All numerical quantities as depicted in A and B are listed.

Furthermore, a comparison of the Q-factors showed that both birdcage coils (@ 17.6 T and 22.3 T) had the highest Q-factors with 500 and 561 respectively, while the solenoid and the saddle coil had lower Q-factors, with 271 and 200 respectively (Fig. 2B and 2C). Approximately a linear increase of the Q-factor is expected for equivalent coils as function of the resonance frequency. The observed deviation in Q-factor indicates that the coil losses of the 5 mm saddle (@ 14.1 T) is higher than in the two 5 mm birdcage coils. The afore-mentioned difference between experimental $SNR_{i,v}$ increase of a factor 5.9 and theoretical value 2.2 can be partially explained by the lower Q-factor of the 5 mm saddle coil (@ 14.1 T).

In an ideal comparison, a theoretical 10-fold increase of volume-normalized $SNR_{i,v}$ is expected when going from a 5 mm birdcage (@ 22.3 T) coil to a 1.5 mm solenoid (@ 22.3 T) coil at the same field strength, due to the decrease in coil diameter (factor 3.3) [10] and changing the geometry from birdcage to solenoid (factor 1:3) [20]. The experimental SNR-increase by comparing the $SNR_{i,v}$ is only a factor of 3.5 and is likely to be explained by a number of factors. First, the theoretical factor due to changing a geometry, which is shown by Hoult and Richards from a saddle to solenoid coil [8], decreases from 3:1 towards a factor 2:1 when a smaller solenoid length to diameter ratio is used, as in the present research. Second, this theoretical geometry is valid for optimized coils in terms of the proximity effect [8], which is not the case in our solenoid coil due to the tighter winding. Third, higher resistance in additional tuning and matching capacitors in the solenoid (Fig. 1C) especially at high frequencies lead to losses in the overall SNR of the coil. A more systematic optimisation of different coil parameters would be needed to conclude if the theoretical improvement factor can be reached.

3.3. Determining the detection limits for metabolites at 22.3 T using 5 mm RF coils

To determine the detection limit of potential metabolites, a localized spectroscopy experiment was performed on the 5 mm birdcage (@ 22.3 T) using a voxel volume of (500 μm)^3, corresponding to 125 nL (Fig. 3). 100 mM of acetate could be detected with 16 averages over a 16 s acquisition time with an SNR of 25:1 (Fig. 3A), while the SNR of 10 mM acetate was slightly above 2:1 using the same parameters (Fig. 3B). When measuring 10 mM acetate with

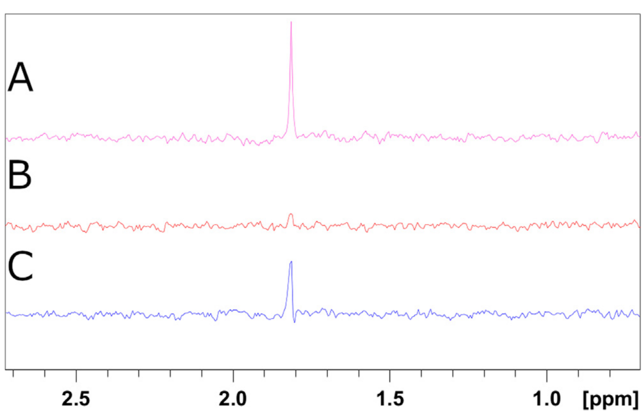

Fig. 3. Localized Spectroscopy (PRESS) on different acetate concentrations at 22.3 T A.) 100 mM acetate and B.) 10 mM acetate on 125 nL in 16 s C.) 10 mM acetate 125 nL in 8 min and 32 s.

512 averages for 8 min and 32 s acquisition time, the peak was visible with an SNR of 12:1 (Fig. 3C).

The ability to detect these low-concentrated metabolites in small volumes enables highly spatially resolved spectroscopy of the spatial heterogeneity of biological specimen < 4 mm.

3.4. Decreased acquisition time at constant spatial resolution

The increased $SNR_{i,v}$ at higher B_0 can also be used to minimize the t_{acq} of the MRI experiment. To enable the direct comparison a piece of Lily root was fixed and a 2D-FLASH experiment as a cross-section through the root was recorded on all three systems using approximately the same slice location in the same sample (Fig. 4). We first recorded the 2D-FLASH on the 22.3 T and obtained an SNR of 12.9 in 8 min and 11 s (Fig. 4C). To obtain a similar SNR_i at identical spatial resolution, we adapted the number of signal averages which resulted acquisition times of 33 min at 17.6 T (Fig. 4B,4D) and 3 h and 17 min at 14.1 T (Fig. 4A, D). Thus, at 22.3 T we can accelerate the same imaging experiment 4 times with respect to 17.6 T and 24 times with respect to the 14.1 T.

Image contrast differs with the contrast between cell walls and cell cytoplasm increasing from 14.1 T to 22.3 T (Fig. 4A-C). The signal is decreased in the cell walls due to shorter T_2^* most likely caused by magnetic susceptibility difference in the cell walls, which have a stronger effect at higher magnetic field strengths [21,22]. While this T_2^* decrease at high field strengths can be a disadvantage for imaging at ultra-high field, in this case, it is favourable for increased contrast and Fig. 4C shows that especially the smaller cells around the xylem bundles are distinguishable at 22.3 T, while they are less apparent in the 14.1 T. Surprisingly, susceptibility artefacts which are expected at a high-field strength seem not to increase towards 22.3 T. The small artefact at the 14.1 T stems most likely from an air bubble as the slice has shifted slightly with respect to the slice at 22.3 T or appeared during sample storage between measurements.

3.5. Spatial resolution achievable using 1.5 mm coil with t_{acq} of 58 h

To estimate the spatial resolution achievable at 22.3 T with using a geometrically well-defined sample, we used a phantom consisting of polymer (PMMA) beads with a diameter of 40 μm (Figure S2) in doped water and the 1.5 mm solenoid coil. The

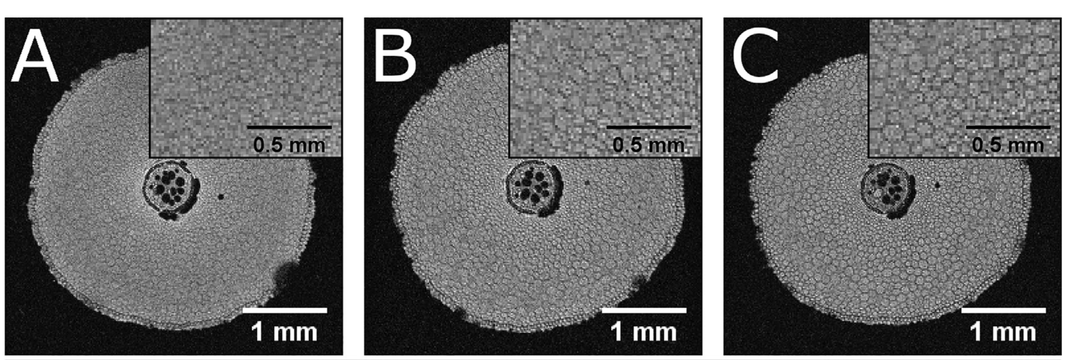

D B_0	14.1 T	17.6 T	22.3 T
Acquisition Time	3 h 17 min	33 min	8 min 11 s
SNR_i	14.2	12.7	12.9

Fig. 4. 2D-FLASH experiments of the same fixed Lily root section at A) 14.1 T B) 17.6 T and C) 22.3 T. The slice position was slightly shifted between the three experiments. The image inserts show an enlarged region of the image. D) The SNR_i and the measurement times demonstrate the much shorter experiment times possible at 22.3 T.

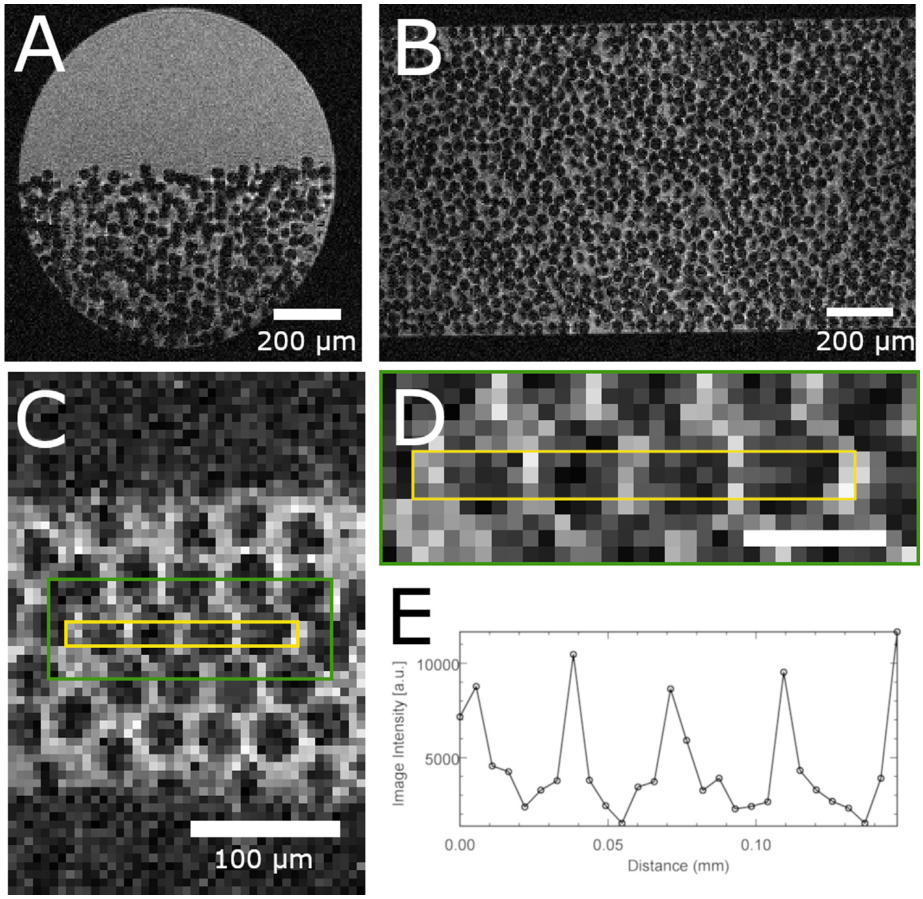

Fig. 5. All images were acquired with a 3D-FLASH experiment with (5.5 μm)^3 isotropic resolution A) One plane of the 3D-FLASH showing the cross-section of the capillary half-filled with PMMA beads B) One plane orthogonal on A) through the centre of the capillary is shown; C) From the same 3D dataset a plane with packed beads at the bottom of the capillary; D) Close-up image of 4 beads (indicated with a green frame in image C, the scale bar corresponds to 50 μm; E) Intensity profile of the cross-section through the beads across the area indicated in C and D with a yellow rectangle. (For the color version of this image, we refer to the web version of the research article)

PMMA beads are densely packed at the bottom of the capillary and less ordered towards the middle of the sample (Fig. 5A). The capillary was not completely filled with beads. An SNR_i of 12 was measured in the top part where only doped water was present (Figure S3). Fig. 5B shows a plane of this 3D-dataset with a nominal resolution (5.5 μm)^3, corresponding to 164 fL. A video of this full 3D-experiment is available (Figure S4). Enhanced image intensity around the beads is observed likely due to diffusion edge enhancement. Small air spaces in the sample in combination with the gradient echo sequence used caused susceptibility effects in the form of a low image intensity. An image plane located at the bottom of the phantom (Fig. 5C) shows that the PMMA beads are ordered due to dense packing and enables the identification of the individual beads. If the intensity across individual beads (Fig. 5D) is plotted, the separation of individual beads can be confirmed (Fig. 5E). However, significant intensity differences over the bead at the right side of the image show that for rigorous data analysis a higher SNR might be needed.

4. Discussion

4.1. Spatial resolution and acquisition times

At the advent of the field of Magnetic Resonance Microscopy, predictions concerning the limits of resolutions stated a 'brick wall' around 10 μm [1] due to sensitivity limitations. To push the limit of resolution, numerous researches have successfully increased SNR by moving to higher B_0 and used highly-sensitive RF microcoils [23–28]. However, these studies have in common that in addition to microcoils, dedicated hardware such as extremely high gradient field strengths up to 65 T/m [23] or low temperatures [24] were utilised, which mitigate resolution limiting factors such as T_2-line broadening and diffusion limitations [10,29]. In this research (Section 3.4), we have demonstrated that a 3D-scan at high resolutions is possible when using a 1.5 mm solenoid coil in combination with a high field strength and standard gradient set of 3 T/m. Our solenoid coil had a larger diameter than those used in previous research and we were able to obtain larger FOVs (1.58 mm × 1.05 mm × 1.05 mm). The key difference is therefore that our setup enables high-resolution 3D MRI measurements at larger FOV and object sizes than previous research [23–28] using standard gradients of 3 T/m for this experiment.

However, the SNR increase by B_0 and detector sensitivity increases will not be sufficient to increase the spatial resolution at our current 22.3 T system further. Linewidth-affecting factors, such as diffusion, T_2-broadening and susceptibility are known to limit the achievable spatial resolution [1,30]. Higher magnetic field gradient strengths mitigate these effects and lead to a lower contribution of these effects to the broadening of the point-spread function [29,31]. Using our current system with a gradient field strength of 3 T/m, the resolution limit is predicted to be around 4 μm [29,31]. Gradient development is an essential component to increase the achievable spatial resolution also at ultra-high field strength B_0. At higher resolution, the true resolution becomes diffusion and T_2 limited [30]. Susceptibility artefacts due to for instance air spaces are a problem at the presented ultra-high field strength of 22.3 T. To this end, pure phase encoding approaches are promising firstly to overcome the resolution limit arising from diffusion and secondly as they suffer less from susceptibility artefacts [32–34]. To approach the optimal resolution close to the resolution limit, additionally multiple echo summation should be considered [1].

4.2. Opportunities and challenges of MRM at ultra-high field strength

The most obvious advantage of using higher field strength is the SNR increase for a given measurement time. This can be conveniently used for faster acquisition, so shortening of the acquisition time with respect to lower-field spectrometers. Furthermore, as the detection limit is lowered by the increased SNR, it can be used for imaging metabolites at tens of mM concentrations in small volumes of interest of 125 nL. In contrast to localized spectroscopy in smaller sample volumes within biological cells which has readily been shown on microcoils [35,36], our results show the possibilities of spatially resolved metabolite detection in a commercial 5 mm coil and therefore its application to larger sample sizes, where the high-field can provide sufficient SNR for metabolite MRM in plant tissues [37,38].

At higher field strength, the T_2 decreases while the T_1 increases. Therefore, MR parameters for acquisition need to be optimised to allow for a short echo time and a longer repetition time for maximum signal acquisition, in case of quantitative measurements. T_2-quantification below 100 μm resolution is dependent on the image resolution [14]. The resolution dependence impedes the quantitative interpretation of high-resolution T_2 maps, and a distinction based on T_2-maps is getting more difficult due to the convergence of apparent T_2 values. As an alternative workaround for high-resolution T_2-experiments at high B_0, T_2-prepared sequences could be used for high resolution quantitative imaging. However, these come with increased measurement time, as only one echo time point could be measured in each repetition time.

Susceptibility effects increase with increasing field strengths, which can lead to positive as well as negative effects. On the one hand, it can decrease T_2^* values of certain tissue types and therefore enhance image contrast, which is beneficial. The T_2^* values decrease towards higher magnetic field strengths caused by mesoscopic magnetic field inhomogeneities in e.g. cell walls can manifest as an advantage due to an increased contrast in the (inevitably) T_2^*-weighted images (see section 3.4) [38]. This could lead to an increased contrast-to-noise ratio comparing two different compartments within a sample. With a suitable sample this could be quantified across different field strength including 22.3 T. On the other hand, macroscopic inhomogeneities caused (e.g. air bubbles) can cause severe image artefacts, and therefore, not all samples are suitable for MRM with frequency-encoded sequences at ultra-high field. Spin-echo sequences are more robust than gradient-echo sequences but are used at the expense of longer t_{acq}. Examples of factors causing susceptibility artefacts are the presence of air spaces in the phantoms or tissues [10] and materials containing paramagnetic ions. Air spaces which cause image artefacts in biological tissues can be resolved by infiltrating the tissue by perfluorodecalin [39]. When imaging an activated carbon granule [40], we also observed strong image artefacts, which are suspected to be due to the paramagnetic ions which are present in the activated carbon granule. Efforts to reduce the amounts of paramagnetic ions have paid off; we could complete this study on 14.1 T but have not yet obtained artefact-free images on 22.3 T. To extend the applicability of ultra-high field, susceptibility free imaging approaches could be tested such as SPEN [41]. Leftin et *al.*[41] showed that DW-SPEN has advantagesover DW-EPI at 21.1 T. Additionally, pure phase encoding approaches such as SE SPI, SPRITE or BLIPPED [32–34] could be evaluated.

5. Outlook and Conclusion

Using the SNR-increase for shorter t_{acq} at 22.3 T offers opportunities for imaging systems in a shorter time and potentially dynamic systems. To improve acquisition times further, combining the ultra-high field with acceleration techniques (e.g. compressed sensing) [42] techniques would be very promising.

To further increase SNR for MRI and MRS at ultra-high field strength, additional methods for sensitivity enhancement could be used. Chemical Exchange Saturation Transfer (CEST) can detect lower concentrations of metabolites as saturation of the exchangeable metabolite protons and the subsequent exchange with water protons lead to a signal amplification over direct localized spectroscopy methods [43]. Higher field strengths are postulated to be advantageous for CEST as the chemical shift dispersion is higher and allows for more selective saturation. Additionally, hyperpolarization techniques such as SABRE [44] and DNP [45] are being developed for *in vivo* MRI application and can lead to promising applications in MRS in the future.

Where will the developments go with ultra-high field MRI when the first magnets above 23.5 T are becoming available? With the current 5 mm diameter coils, we do not expect B_1-inhomogeneity problems due to interference, which is a challenge at high-field MRI for medical applications. The SNR increase expected at this field strength will certainly enable to image with a higher spatial and shorter acquisition time which will be advantageous for numerous applications. However, we do not expect to breach the resolution limit of $(5\ \mu m)^3$ considerably as this resolution limit is the regime where it is limited by the maximum gradient strength of the currently commercially available gradient strengths on NMR spectrometer systems [29]. Furthermore, coil development and dedicated setups are highly recommended for smaller samples (d < 3 mm).

Using a 22.3 T magnetic field strengths we have shown that a 5.9-fold increase of the volumetric SNR can be achieved compared to the 14.1 T using 5 mm commercial volume coils at the respective systems. When using a home-built 1.5 mm solenoid coil, this further increases with a factor 3.5 with respect to the 5 mm volume coil at the 22.3 T. This $SNR_{i,v}$ increase can be used for faster imaging, lower spin concentrations in localised spectroscopy or increasing the spatial resolution until the resolution limit. Spatial resolution of down to $(5.5\ \mu m)^3$ using a standard gradient set and a large FOV demonstrate the opportunities for high-resolution MRI with larger specimens. The detection limits on localized spectroscopy in a 5 mm birdcage show the potential of using ultra-high field MRI for metabolite detection. In future, a combination with additional sensitivity enhancement techniques could open the field of MRM to a wider range of spatially resolved metabolite imaging applications.

Declaration of Competing Interest

The authors declare that they have no known competing financial interests or personal relationships that could have appeared to influence the work reported in this paper.

Acknowledgements

J.R.K. was supported by the NWO-funded Netherlands' Magnetic Resonance Research School (NMARRS) graduate school [022.005.029]. R.v.S. was supported by funds from grants from BioSolar Cell (U2.3) consortium which is supported by Dutch ministry of economic affairs. Experiments at the 950 MHz instrument were supported by uNMR-NL, an NWO-funded National Roadmap Large-Scale Facility of the Netherlands [184.032.207]. We thank Klaartje

Houben, Johan van der Zwan and Marie Renault for technical support at the uNMR-NL facility, Pieter de Waard and John Philippi for technical support at the MAGNEFY center and Karthick B. Sai Sankar Gupta for technical support at Leiden University. We thank Prof. Arno Kentgens for valuable discussions.

Appendix A. Supplementary material

Supplementary data to this article can be found online at https://doi.org/10.1016/j.jmr.2020.106770.

References

[1] P.T. Callaghan, Principles of Nuclear Magnetic Resonance Microscopy, Oxford University Press, 1993.
[2] W. Kuhn, NMR microscopy—fundamentals, limits and possible applications, Angew. Chem. Int. Ed. 29 (1990) 1–19, https://doi.org/10.1002/anie.199000013.
[3] S.J. Blackband, D.L. Buckley, J.D. Bui, M.I. Phillips, NMR microscopy-–beginnings and new directions, Magn. Reson. Mater. Physics, Biol. Med. 9 (1999) 112–116, https://doi.org/10.1007/BF02594606.
[4] A.R. Kherlopian, T. Song, Q. Duan, M.A. Neimark, M.J. Po, J.K. Gohagan, A.F. Laine, A review of imaging techniques for systems biology, BMC Syst. Biol. 2 (2008) 74.
[5] B. Driehuys, J. Nouls, A. Badea, E. Bucholz, K. Ghaghada, A. Petiet, L.W. Hedlund, Small animal imaging with magnetic resonance microscopy, ILAR J. 49 (2008) 35–53, https://doi.org/10.1093/ilar.49.1.35.
[6] Y. Xia, J.B. Moody, N. Burton-Wurster, G. Lust, Quantitative in situ correlation between microscopic MRI and polarized light microscopy studies of articular cartilage, Osteoarthr. Cartil. 9 (2001) 393–406, https://doi.org/10.1053/joca.2000.0405.
[7] A. Webb, Increasing the sensitivity of magnetic resonance spectroscopy and imaging, Anal. Chem. 84 (2012) 9–16, https://doi.org/10.1021/ac201500v.
[8] D.I. Hoult, R.E. Richards, The signal-to-noise ratio of the nuclear magnetic resonance experiment, J. Magn. Reson. 24 (1976) 71–85, https://doi.org/10.1016/j.jmr.2011.09.018.
[9] K.R. Minard, R.A. Wind, Picoliter 1H NMR spectroscopy, J. Magn. Reson. 154 (2002) 336–343. https://doi.org/10.1006/jmre.2001.2494.
[10] L. Ciobanu, in: Microscopic Magnetic Resonance Imaging: A Practical Perspective, Pan Stanford Publishing, 2017, https://doi.org/10.1201/9781315107325.
[11] A.G. Webb, Radiofrequency microcoils in magnetic resonance, Prog. Nucl. Magn. Reson. Spectrosc. 31 (1997) 1–42, https://doi.org/10.1016/S0079-6565(97)00004-6.
[12] M.T. Vlaardingerbroek, J.A. Boer, Magnetic Resonance Imaging: Theory and Practice, Springer Science & Business Media, 2013.
[13] P. Mansfield, P.G. Morris, NMR Imaging in Biomedicine, Academic Press, New York, 1982.
[14] H.T. Edzes, D. van Dusschoten, H. Van As, Quantitative T2 imaging of plant tissues by means of multi-echo MRI microscopy, Magn. Reson. Imaging. 16 (1998) 185–196. https://doi.org/10.1016/S0730-725X(97)00274-9.
[15] T. Oerther, Manual - Micro Imaging for AVANCE III Systems User Guide Version 001, 2012.
[16] J. Schindelin, I. Arganda-Carreras, E. Frise, V. Kaynig, M. Longair, T. Pietzsch, S. Preibisch, C. Rueden, S. Saalfeld, B. Schmid, Fiji: an open-source platform for biological-image analysis, Nat. Methods 9 (2012) 676.
[17] H. Benveniste, G. Einstein, K.R. Kim, C. Hulette, G.A. Johnson, Detection of neuritic plaques in Alzheimer's disease by magnetic resonance microscopy, Proc. Natl. Acad. Sci. 96 (1999) 14079–14084, https://doi.org/10.1073/pnas.96.24.14079.
[18] H. Benveniste, S. Blackband, MR microscopy and high resolution small animal MRI: Applications in neuroscience research, Prog. Neurobiol. 67 (2002) 393–420, https://doi.org/10.1016/S0301-0082(02)00020-5.
[19] A. Haase, F. Odoj, M. Von Kienlin, J. Warnking, F. Fidler, A. Weisser, M. Nittka, E. Rommel, T. Lanz, B. Kalusche, M. Griswold, NMR probeheads for in vivo applications, Concepts Magn. Reson. 12 (2000) 361–388, https://doi.org/10.1002/1099-0534(2000)12:6<361::AID-CMR1>3.0.CO;2-L.
[20] J. Mispelter, M. Lupu, A. Briguet, NMR Probeheads for Biophysical and Biomedical Experiments: Theoretical Principles & Practical Guidelines, Imperial College Press, 2006.
[21] R.W. Brown, E.M. Haacke, Y.-C.N. Cheng, M.R. Thompson, R. Venkatesan, Magnetic Resonance Imaging: Physical Principles and Sequence Design, John Wiley & Sons, 2014.
[22] D.A. Yablonskiy, E.M. Haacke, Theory of NMR signal behavior in magnetically inhomogeneous tissues: the static dephasing regime, Magn. Reson. Med. 32 (1994) 749–763.
[23] M. Weiger, D. Schmidig, S. Denoth, C. Massin, F. Vincent, M. Schenkel, M. Fey, NMR microscopy with isotropic resolution of 3.0 μm using dedicated hardware and optimized methods, Concepts Magn. Reson. Part B Magn. Reson. Eng. 33B (2008) 84–93, https://doi.org/10.1002/cmr.b.20112.
[24] H.Y. Chen, R. Tycko, Low-temperature magnetic resonance imaging with 2.8 μm isotropic resolution, J. Magn. Reson. 287 (2018) 47–55, https://doi.org/10.1016/j.jmr.2017.12.016.
[25] E. Moore, R. Tycko, Micron-scale magnetic resonance imaging of both liquids and solids, J. Magn. Reson. 260 (2015) 1–9, https://doi.org/10.1016/j.jmr.2015.09.001.
[26] S.C. Lee, K. Kim, J. Kim, J.H. Yi, S. Lee, C. Cheong, MR microscopy of micron scale structures, Magn. Reson. Imaging. 27 (2009) 828–833, https://doi.org/10.1016/j.mri.2009.01.002.
[27] S.C. Lee, K. Kim, J. Kim, S. Lee, H.Y. Jeong, W.K. Sung, K.S. Ha, C. Cheong, One micrometer resolution NMR microscopy, J. Magn. Reson. 150 (2001) 207–213, https://doi.org/10.1006/jmre.2001.2319.
[28] L. Ciobanu, D. Seeber, C. Pennington, 3D MR microscopy with resolution 3.7 um by 3.3 um by 3.3 um, J. Magn. Reson. 158 (2002) 178–182, https://doi.org/10.1016/S1090-7807(02)00071-X.
[29] A.G. Webb, Optimizing the point spread function in phase-encoded magnetic resonance microscopy, Concepts Magn. Reson. 22A (2004) 25–36, https://doi.org/10.1002/cmr.a.20010.
[30] P.T. Callaghan, C.D. Eccles, Diffusion-limited resolution in nuclear magnetic resonance microscopy, J. Magn. Reson. 78 (1988) 1–8. https://doi.org/10.1016/0022-2364(88)90151-5.
[31] T. Neuberger, A. Webb, Radiofrequency coils for magnetic resonance microscopy, NMR Biomed. 22 (2009) 975–981, https://doi.org/10.1002/nbm.1246.
[32] I.V. Mastikhin, B.J. Balcom, Centric SPRITE MRI of Biomaterials with Short T_2*, Encycl. Magn. Reson. 1 (2012) 783–788, https://doi.org/10.1002/9780470034590.emrstm1265.
[33] D. Xiao, B.J. Balcom, Restricted k-space sampling in pure phase encode MRI of rock core plugs, J. Magn. Reson. 231 (2013) 126–132, https://doi.org/10.1016/j.jmr.2013.04.001.
[34] D. Xiao, B.J. Balcom, BLIPPED (BLIpped Pure Phase EncoDing) high resolution MRI with low amplitude gradients, J. Magn. Reson. 285 (2017) 61–67, https://doi.org/10.1016/j.jmr.2017.10.013.
[35] S.C. Grant, N.R. Aiken, H.D. Plant, S. Gibbs, T.H. Mareci, A.G. Webb, S.J. Blackband, NMR spectroscopy of single neurons, Magn. Reson. Med. 44 (2000) 19–22, https://doi.org/10.1002/1522-2594(200007)44:1<19::AID-MRM4>3.0.CO;2-F.
[36] S.-C. Lee, J.-H. Cho, D. Mietchen, Y.-S. Kim, K.S. Hong, C. Lee, D. Kang, K.D. Park, B.-S. Choi, C. Cheong, Subcellular in vivo 1H MR spectroscopy of Xenopus laevis oocytes, Biophys. J. 90 (2006) 1797–1803.
[37] W. Köckenberger, Nuclear magnetic resonance micro-imaging in the investigation of plant cell metabolism, J. Exp. Bot. 52 (2001) 641–652.
[38] M. Musse, H. Van As, NMR imaging of air spaces and metabolites in fruit and vegetables, Mod. Magn. Reson. (2018) 1765–1779, https://doi.org/10.1007/978-3-319-28388-3_130.
[39] R. van Schadewijk, J.R. Krug, D. Shen, K.B.S.S. Gupta, F.J. Vergeldt, T. Bisseling, A. G. Webb, H. Van As, A.H. Velders, H.J.M. de Groot, Magnetic resonance microscopy at cellular resolution and localised spectroscopy of medicago truncatula at 22.3 tesla, Sci. Rep. 10 (2020) 1–11.
[40] L. Caizán-Juanarena, J.R. Krug, F.J. Vergeldt, J.M. Kleijn, A.H. Velders, H. Van As, A. ter Heijne, 3D biofilm visualization and quantification on granular bioanodes with magnetic resonance imaging, Water Res. 115059 (2019).
[41] A. Leftin, J.T. Rosenberg, E. Solomon, F.C. Bejarano, S.C. Grant, L. Frydman, Ultrafast in vivo diffusion imaging of stroke at 21.1 T by spatiotemporal encoding, Magn. Reson. Med. 73 (2015) 1483–1489, https://doi.org/10.1002/mrm.25271.
[42] J. Tsao, S. Kozerke, MRI temporal acceleration techniques, J. Magn. Reson. Imaging. 36 (2012) 543–560.
[43] P.C.M. van Zijl, N.N. Yadav, Chemical exchange saturation transfer (CEST): What is in a name and what isn't?, Magn. Reson. Med. 65 (2011) 927–948, https://doi.org/10.1002/mrm.22761.
[44] J.-B. Hövener, N. Schwaderlapp, T. Lickert, S.B. Duckett, R.E. Mewis, L.A.R. Highton, S.M. Kenny, G.G.R. Green, D. Leibfritz, J.G. Korvink, A hyperpolarized equilibrium for magnetic resonance, Nat. Commun. 4 (2013) 2946.
[45] M.S. Vinding, C. Laustsen, I.I. Maximov, L.V. Søgaard, J.H. Ardenkjær-Larsen, N. C. Nielsen, Dynamic nuclear polarization and optimal control spatial-selective 13C MRI and MRS, J. Magn. Reson. 227 (2013) 57–61.